Graphene Saturable Absorber Mirrors for Silicon Photonic Platforms

Dimitrios Chatzidimitriou, Dimitrios C. Zografopoulos, and Emmanouil E. Kriezis, *Senior Member, IEEE*

***Abstract*—We employ graphene saturable absorption for the theoretical demonstration of saturable absorption mirrors based on planar silicon photonic Bragg gratings. Two geometries are investigated, that of a silicon wire grating and a silicon slot grating, showcasing the increased light-matter interaction of the high-confinement slot waveguide. The gratings are designed in the linear regime for single mode operation, low footprint and broadband operation in the near infrared optical communications frequency range. The saturable absorption effect is introduced through the saturation of graphene's interband surface conductivity, and we discuss the necessary biasing conditions and applicability of our CW approach on ps-long pulses. We also rigorously include other, possibly detrimental, nonlinear effects, such as silicon's Kerr effect and two photon absorption, and graphene's Kerr effect. These effects are proven to have a negligible impact on the operation of the graphene saturable absorber mirror, thanks to the much lower power threshold of graphene's saturable absorption. Finally, we calculate the nonlinear reflectance and transmittance of the graphene-enhanced Bragg gratings and demonstrate that they can provide high modulation depths at low saturation powers, both highly valued characteristics of saturable absorber mirrors for mode locking applications in view of next-generation integrated pulsed photonic light sources.**

***Index Terms*—Bragg gratings, integrated optics, mode locked lasers, optical planar waveguide components, nonlinear optics, Graphene, saturable absorber mirrors, silicon on insulator technology.**

I. INTRODUCTION

NANOPHOTONICS has been in the forefront of photonics research for the past decade, being a constant driving force for the photonics integrated circuit (PIC) industry. Specifically silicon photonics, due to their high technological maturity level and CMOS compatibility, have provided an ideal platform for photonic components in the near infrared optical communications spectrum [1]. However, the development of low-cost efficient light sources that can directly lase into silicon single mode waveguides is yet to be truly realized. One of the most promising solutions for integrated light sources for silicon on insulator platforms is the development of silicon organic hybrid waveguides with the use of dye-doped optical organic materials [2]–[5]. Towards this direction, conversion of CW sources to pulsed emission must also be realized in a compatible platform that does not require costly fabrication techniques.

One of the most commonly and widely used techniques for pulsed emission is mode-locking and an integral part of any mode-locking scheme is the saturable absorber. Graphene has been successfully used in an abundance of mode-locking applications, especially in fiber lasers [6], [7]. This was made possible thanks to graphene's saturable absorption that exhibits very low saturation intensity as well as ultra-fast carrier dynamics [8], [9]. Furthermore, graphene's 2D geometry allows for seamless integration with well-studied photonic devices, especially in the near infrared spectral region [10]. Due to these advantages, graphene's SA has been and still is the subject of intense research [11]. In early works, graphene sheets were placed on the cross-section of a fiber connection [12]–[14], and the small absorption modulation that it provided was enough to passively mode-lock or Q-switch the fiber laser [15], [16]. Later works focused on increasing the interaction length with graphene and thus the sheets were placed such that they (optimally) overlap with the evanescent field of a tapered fiber [17]–[19], on the polished side of D-shaped fibers [20]–[22], and finally incorporated into photonic waveguides to maximize the light-matter interaction [23]–[27]. Bragg gratings and 1-D photonic crystals have also been studied [28], although works have focused primarily on the Kerr effect to shift the resonant frequency [29], [30] or used patterned graphene sheets to form the Bragg grating itself [31]. Beyond fiber lasers, several studies have reported the experimental mode-locking and Q-switching of VECSELs [32] and solid-state lasers [33]–[35] with graphene saturable absorber mirrors (GSAMs). In these works, graphene layers were transferred on the surface of a mirror or sandwiched in multi-layered structures. A major concern of such implementations is the poor interaction length with the 2D material (which leads to low modulation depths), the latter being the result of the graphene placement on the plane normal to the propagation direction.

In this work, we introduce a GSAM based on silicon photonic Bragg gratings, with the proposed design being the contemporary counterpart of the earlier GSAMs. Our aim is to use existing low-cost planar silicon photonic structures that can provide superior light-matter interaction with graphene and thus operate as broadband, low-power mode locking elements for standing wave

---

Manuscript received 28 June 2022; accepted 29 June 2022. Date of publication 4 July 2022; date of current version 15 July 2022. The research work was supported by the Hellenic Foundation for Research and Innovation (HFRI) under the "First Call for HFRI Research Projects to support Faculty members and Researchers and the procurement of high-cost research equipment grant" (Project No. HFRI-FM17-2086). *(Corresponding author: Dimitrios Chatzidimitriou.)*

Dimitrios Chatzidimitriou and Emmanouil E. Kriezis are with the School of Electrical and Computer Engineering, Faculty of Telecommunications, Aristotle University of Thessaloniki, 54124 Thessaloniki, Greece (e-mail: dchatzid@auth.gr; mkriezis@auth.gr).

Dimitrios C. Zografopoulos is with the Consiglio Nazionale delle Ricerche - Istituto per la Microelettronica e Microsistemi, 00133 Rome, Italy (e-mail: dimitrios.zografopoulos@artov.imm.cnr.it).

Digital Object Identifier 10.1109/JPHOT.2022.3188222

integrated photonic sources, such as state of the art silicon organic hybrid on-chip lasers [2], [5], [36]. To this end, we employ two silicon on insulator (silicon oxide) photonic Bragg gratings based on established single-mode silicon wire and slot waveguides. The wire waveguide is employed as a low-confinement waveguide, in contrast to the slot waveguide which has higher confinement and light-matter interaction [37]. The gratings are formed by periodically etching air holes in the waveguides, which are then filled with Poly(methyl methacrylate) (PMMA) to planarize the whole structure. A graphene monolayer is placed on the top face of the grating. The gratings are theoretically designed so that the photonic bandgap is centered at the 1550 nm wavelength. The design is verified by full-wave 3D frequency-domain simulations of the Bragg gratings, producing the linear transmission/reflection spectra and dispersion diagrams. We then rigorously include in our model the silicon nonlinear effects that could potentially prove detrimental to such a design, specifically the Kerr and two photon absorption (TPA) effects, as well as the graphene Kerr effect. Graphene's SA is then introduced as the saturation of graphene's interband conductivity. We provide in-depth details for our choice of assumptions, parameters and design choices, while also arguing that our CW analysis can be readily used for ps-long pulses. Finally, with the inclusion of all relevant nonlinear effects we calculate the nonlinear reflectance and transmittance of the designed GSAMs, showcasing their high reflectance modulation, low insertion losses, and low saturation power. To the best of our knowledge, graphene saturable absorber mirrors have never been studied before in the context of Bragg gratings written in silicon and this work presents their high potential for use in integrated on-chip sources.

The article is organized as follows: Section II discusses the material linear properties and the linear Bragg design. Section III provides the nonlinear material properties of silicon and graphene, namely the Kerr effect, TPA and SA. Section IV investigates the nonlinear properties/dependence of the GSAM reflectance and transmittance, as well as the comparison between them. Finally, Section V provides the conclusions of this work.

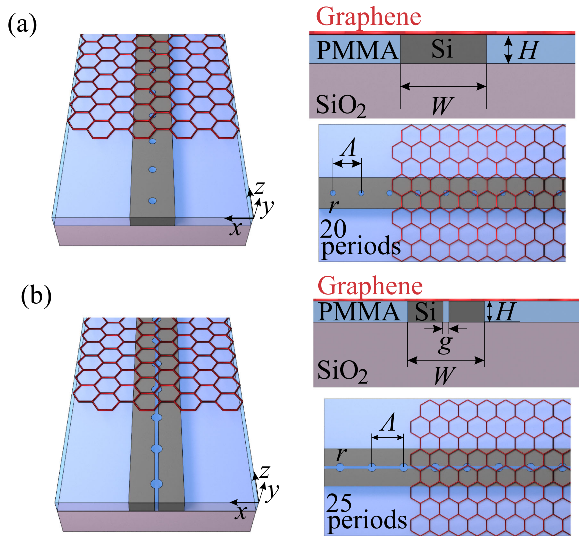

Fig. 1. (a) Silicon wire Bragg grating with graphene in 3D perspective as well as the xy cross section and xz top view. All materials and relevant dimensions that are used in the text are also depicted in the figures. (b) Silicon slot Bragg grating with graphene in 3D perspective as well as the xy cross section and xz top view. Note that the absence of graphene for the first few Bragg periods is for visualization and clarity purposes only.

II. BRAGG MIRROR DESIGN IN THE LINEAR REGIME

A. *Waveguide Design and Linear Material Properties*

The Bragg gratings are based on a silicon wire and a silicon slot waveguide, as seen in Fig. 1(a) and (b), respectively. The silicon waveguides are patterned on top of a silicon oxide substrate, in a standard silicon-on-insulator (SOI) configuration, and the whole structure is planarized with PMMA. Finally, a graphene monolayer is deposited directly on the top face of the waveguides as in Fig. 1, where the absence of graphene coating in the first few periods is for visualization purposes only. The periodic variation of the effective refractive index of the photonic mode is achieved by opening air holes in the waveguide. The holes are subsequently filled with PMMA during the planarization process.

The bulk materials used, at the wavelength of 1550 nm, are modeled through their refractive index. Specifically, we used $n_{\text{Si}} = 3.478$, $n_{\text{SiO}_2} = 1.45$, and $n_{\text{PMMA}} = 1.477$. Material dispersion is included for the silicon and silicon oxide through the respective Sellmeier formulas (see Appendix A). The graphene 2D monolayer is modeled as a boundary condition through its surface conductivity

$$\sigma = \sigma_{\text{inter}} + \sigma_{\text{intra}}, \tag{1}$$

where σ is the total graphene surface conductivity, σ_{inter} is the interband contribution, and σ_{intra} is the intraband contribution. Generally, σ is a strong function of the chemical potential μ_c, since for $\mu_c > \hbar\omega/2$ interband electronic transitions are prohibited and graphene becomes transparent. In the THz region, intraband transitions usually dominate [38] while in the optical regime interband transitions are more important. Formulas for the calculation of the graphene conductivity can be found in [39]. Because in this work we aim to exploit the saturation of interband losses, we will assume that graphene is a pristine sample, i.e., $\mu_c = 0$ which leads to $\sigma_{\text{inter}} \approx 60.9\,\mu\text{S}$ and $\sigma_{\text{intra}} \approx 0$, ideally for all frequencies due to graphene's linear band structure. In a more realistic scenario where the graphene sample is not pristine, an electrostatic control bias can be used [40] to set μ_c very close to zero and any small deviations will have a negligible effect in the NIR frequency range. Furthermore, for normal-quality grown graphene a typical value of μ_c can be $\sim 200\,\text{meV}$, which still has a small intraband contribution [41]. See Appendix A and Fig. 6 for more details. Graphene's surface current density can be written in the frequency domain as

$$\mathbf{J}_s = \sigma \mathbf{E}_{\parallel}. \tag{2}$$

Note that only the parallel to the graphene sheet electric field $\mathbf{E}_{\parallel}$ is included in (2) [23].

The waveguide dimensions are chosen so that single mode operation is supported at any cross-section of the Bragg reflector (i.e. both inside and outside the holes), the device is compact, the mode has a quasi-TE polarization with the dominant components in the x and z directions (thus enabling a strong interaction with graphene), and finally radiation losses are minimized. For the silicon wire case we chose the width $W = 450$ nm, height $H = 150$ nm and the radius of the holes $r = 40$ nm. For the silicon slot waveguide the dimensions are $W = 550$ nm, $H = 150$ nm, slot gap $g = 40$ nm, and $r = 60$ nm.

To find the Bragg period Λ at 1550 nm we use the well-established Bragg condition

$$N\pi = \bar{n}_{\text{eff}} k_0 \Lambda, \tag{3}$$

where N is order of the Bragg grating, k_0 is the free space wave number and $\bar{n}_{\text{eff}}$ is the effective refractive index of the guided mode, averaged over the period Λ. The averaged effective index was calculated for the central wavelength of 1550 nm by Finite Element Method (FEM) based mode analysis of the cross sections of the waveguide and (3) was solved semi-analytically, leading to $\Lambda = 410$ nm and $\Lambda = 460$ nm for the wire and slot waveguides, respectively. To keep the reflector as compact as possible we choose $N = 1$.

The fabrication of the bus waveguides and Bragg gratings can be achieved either with standard 193 nm optical lithography and dry etching [37] or with electron beam lithography and deep reactive-ion etching [42]. The PMMA cladding can be spin-coated, completely filling all the gaps as demonstrated in [36]. Chemical vapor deposition (CVD) grown monolayer graphene can be deposited onto the photonic chips through the wet-transfer method [37], [42], [43].

B. Linear Spectra and Dispersion Diagrams

In Fig. 2(a) we plot the S-parameters $|S_{11}|^2$ (reflectance) and $|S_{21}|^2$ (transmittance) for the silicon wire Bragg grating of Fig. 1(a) with 20 periods. Ports 1 and 2 are at the physical start and end of the grating, respectively, and they refer to the guided mode. The parameters were calculated by 3D FEM full-wave analysis of the Bragg grating, including all relevant material dispersion effects. As insets we plot on the right the norm of the electric field $|\mathbf{E}|$ of the TE polarized mode (xy cross section) at 1550 nm. In the bottom we also plot the electric field norm, again at 1550 nm, in the xz plane. As a final verification, Fig. 2(b) shows the dispersion diagram (wavelength vs the Floquet wave vector) for the unit cell of the Bragg grating, where we can clearly notice the presence of the photonic bandgap, in full agreement to Fig. 2(a).

The bandwidth of the silicon wire Bragg grating is calculated from Fig. 2(a) by finding the 3 dB drop points for the reflectance, which results in a broadband reflectance spectrum of about 65.6 nm. Note that the maximum reflectance is around -1 dB, even though we used 20 periods for the Bragg grating. This is a direct consequence of the graphene induced losses. These losses will be saturated by graphene's SA in our subsequent nonlinear analysis with the introduction of the relevant nonlinear effects. The number of periods was chosen so that in the absence of graphene the grating acts as an almost perfect mirror. Thus, the maximum reflection/loss modulation that we can expect is 1 dB, which is sufficiently large for mode locking applications [44]. Finally, in Fig. 2(b) we plot the dispersion diagram of the unit cell of the grating. By comparing the bandgap with the reflectance/transmittance spectra of Fig. 2(a), we can conclude that the single graphene monolayer biased at $\mu_c = 0$ does not have any significant role in the waveguiding process and its impact is solely the introduction of losses.

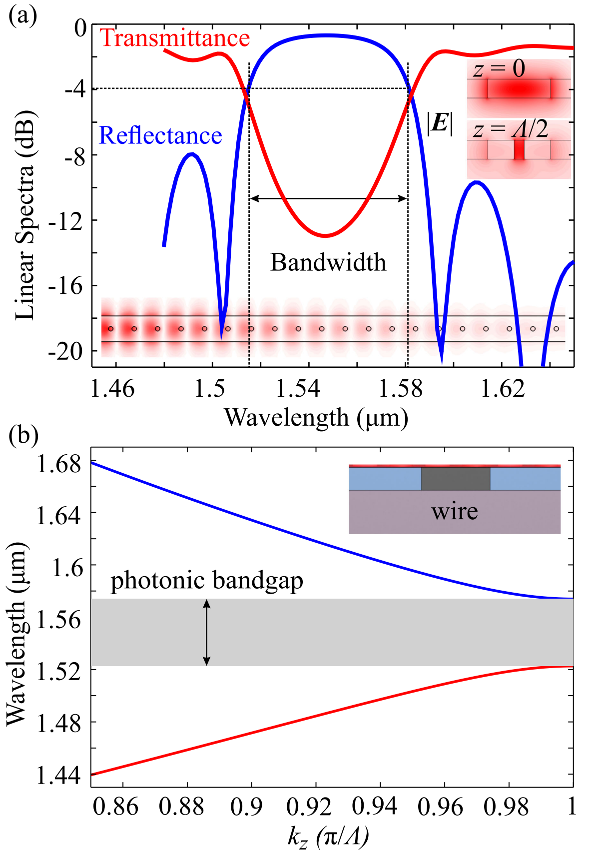

Fig. 2. (a) Linear spectra (reflectance and transmittance) for the silicon wire GSAM. On the top right there are insets of the electric field norm of the TE photonic mode profile (xy cross-section) at $z = 0$ (no hole present) and $z = \Lambda/2$ (at the center of a hole). On the bottom, the inset shows the electric field norm (xz cross-section) at the middle of the bandgap (1550 nm). Also shown is the 3 dB bandwidth for the reflectance. (b) Dispersion diagram for the unit cell of the Bragg grating: wavelength versus the Floquet k_z wave number, showing the photonic bandgap. Different colors signify the different modes.

We follow the same analysis for the silicon slot waveguide grating. Fig 3(a) shows the reflectance and transmittance linear spectra for a 25-period grating, and the insets on the right show the TE mode profiles at two characteristic positions, and on the bottom the CW field distribution at the middle of the bandgap. Fig 3(b) plots the dispersion diagram for the unit cell of the silicon slot waveguide (note that graphene does not impact the linear response), were again the opening of the photonic

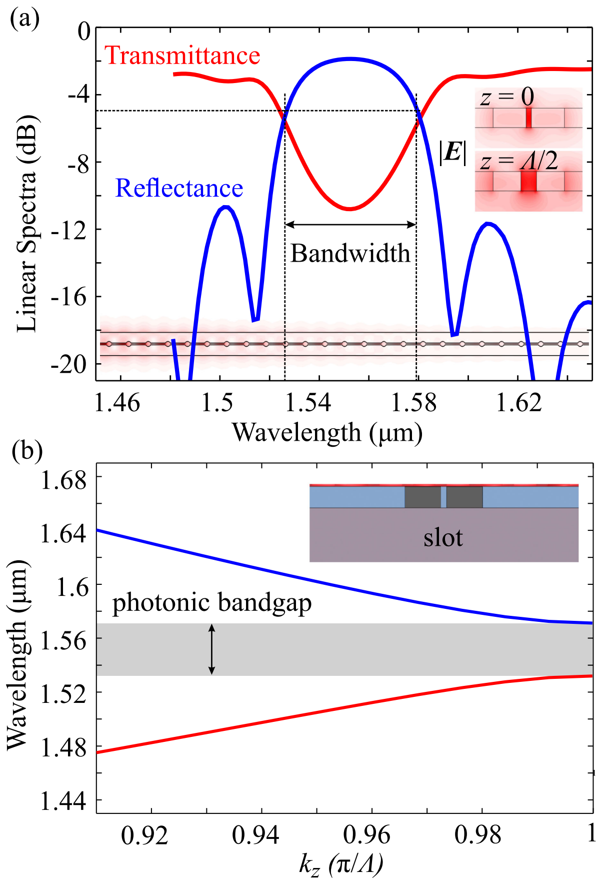

Fig. 3. (a) Linear spectra (reflectance and transmittance) for the silicon slot GSAM, following the same layout as Fig. 2. (b) Dispersion diagram for the unit cell of the Bragg grating: wavelength versus the Floquet k_z wave number. Different colors signify the different modes.

bandgap becomes very evident. There are two important differences, when compared to the silicon wire case. First the bandgap/bandwidth is smaller, calculated in the slot case to approximately 52.6 nm. Although the bandwidth drops about 10 nm, the response is still extremely broadband and suitable for ultrashort pulse generation. Secondly, the maximum reflectance is lower, around -2 dB for the slot case. This can be understood by comparing the mode profiles at $z = 0$: the slot mode is tightly confined in the slot region and thus the x-polarized component interacts strongly with the graphene. On the other hand, the mode profile of the wire waveguide extends to the whole silicon area and has its maximum in the middle of the silicon wire, which is relatively far from graphene. As a result, the stronger light-graphene interaction in the slot waveguide results in increased graphene induced losses [45], which lead to higher reflectance modulation. The drawback is that an integrated mode locked laser design should provide enough gain per round trip to counteract the increased low-power (linear) IL to start the lasing process. Finally, note that the silicon slot grating consists of 25 periods, compared to the wire case where we used 20 periods. The increased number of periods are needed because the effective index contrast in the slot case is lower than the wire case, which can be intuitively understood from the mode profiles in Fig 2(a) and Fig. 3(a).

III. NONLINEAR MATERIAL PROPERTIES

This section contains the models for the dominant nonlinearities that are present in the investigated structures, namely silicon's Kerr effect and TPA, and graphene's Kerr effect and saturable absorption.

Silicon's nonlinearities are implemented through the straightforward and well-documented third order nonlinear permittivity $\chi^{(3)}$. Silicon's nonlinear refractive index $n_2 = 2.5\,\mathrm{m}^2/\mathrm{W}$ is related to the only independent component $\chi^{(3)}_{xxxx}$ of the $\chi^{(3)}$ tensor [46] (assuming full symmetry) through the relation

$$\chi^{(3)}_{xxxx} = \frac{4}{3} n_{\mathrm{Si}}^2 \varepsilon_0 c_0 (1 - j r_{\mathrm{TPA}}) n_2, \tag{4}$$

where c_0 is the vacuum speed of light, ε_0 the vacuum electric permittivity, and r_{TPA} the ratio of Kerr to TPA effects, taken $r_{\mathrm{TPA}} = 0.25$ here [47]. Both the Kerr and TPA effect are then included in our model for CW excitation through the third order nonlinear polarization $\mathbf{P}_{\mathrm{NL}}$ as

$$\mathbf{P}_{\mathrm{NL}} = \frac{1}{4} \varepsilon_0 \chi^{(3)}_{xxxx} (2|\mathbf{E}|^2 \mathbf{E} + \mathbf{E}^2 \mathbf{E}^*), \tag{5}$$

which is then added to the linear polarization in Maxwell's equations:

$$\mathbf{P} = \varepsilon_0 \varepsilon_r \mathbf{E} + \mathbf{P}_{\mathrm{NL}}. \tag{6}$$

Note that (5) and (6) are written in the frequency domain assuming CW excitation at a frequency ω_0.

Graphene's Kerr effect is included in a similar way, through the third order nonlinear surface conductivity $\sigma^{(3)}$ and the respective third order nonlinear current [23]

$$\mathbf{J}_{\mathrm{NL}} = \frac{1}{4} \sigma^{(3)}_{xxxx} (2|\mathbf{E}_{\parallel}|^2 \mathbf{E}_{\parallel} + \mathbf{E}_{\parallel}^2 \mathbf{E}_{\parallel}^*), \tag{7}$$

where we again assumed all possible symmetries for the $\sigma^{(3)}$ tensor and that only the electric field parallel to the graphene monolayer interacts with it. The value of $\sigma^{(3)}_{xxxx} = -j1.57 \cdot 10^{-21}\,\mathrm{Sm}^2/\mathrm{V}^2$ corresponds to a de-focusing effect, opposite that of silicon [48]. We underline here, that $\sigma^{(3)}$ is a function of μ_c and can change both in sign and magnitude for different values of the chemical potential [25]. In this work all graphene properties are calculated at 1550 nm and $\mu_c = 0$. We repeat that the latter assumption is satisfied by a high quality (mechanically exfoliated) graphene sample or with external electrostatic biasing that will set the chemical potential very close to the Dirac point [25]. Furthermore, by assuming that $\mu_c \approx 0$ it also possible to ignore dispersion effects for the linear and nonlinear graphene conductivities in the frequency range we are interested in (1500 nm-1600 nm). Even if graphene's μ_c is not perfectly set to zero, but is very close to it, graphene properties in the NIR can still be approximated very well as dispersionless.

The SA effect, which is the critical property in the GSAM functionality, is modeled by altering (2) as

$$\mathbf{J}_{\mathrm{s}} = \sigma_{\mathrm{intra}} \mathbf{E}_{\parallel} + \frac{\sigma_{\mathrm{inter}}}{1 + \dfrac{|\mathbf{E}_{\parallel}|^2}{E_{\mathrm{sat}}^2}} \mathbf{E}_{\parallel}, \tag{8}$$

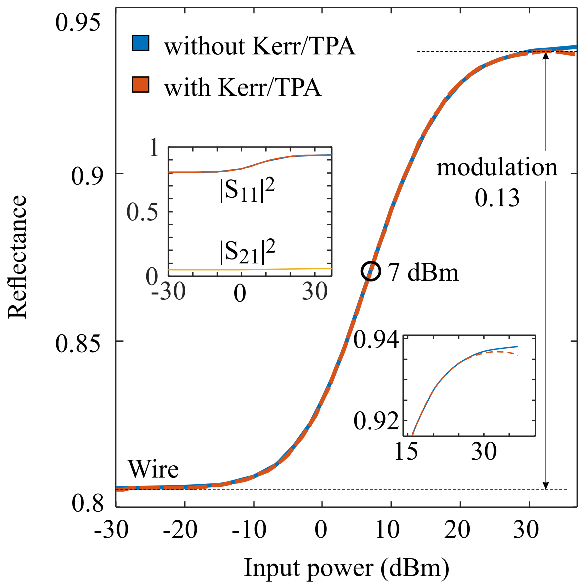

Fig. 4. Nonlinear reflectance of the silicon wire GSAM versus input power. Blue solid curves show the reflectance without Kerr/TPA and red curves with Kerr/TPA. Blue and red curves coincide for input powers up to 35 dBm, when the silicon TPA effect becomes noticeable. This is more clearly seen in the bottom inset which is a zoom-in of the main plot. The top left inset also shows the transmittance, which has negligible variation with input power. The midpoint between the minimum and maximum reflectance is denoted with a black circle, and next to it we note the saturation power of the GSAM.

where the saturation electric field is given

$$E_{\text{sat}}^2 = 2Z_0 I_{\text{sat}}, \tag{9}$$

with $Z_0 = 120\pi\,\Omega$ being the free space impedance and I_{sat} the saturation intensity having the value of $1\,\text{MW/cm}^2$ from experimental and theoretical measurements [12]. Although the value chosen for I_{sat} is acceptable, values as high as $100\,\text{MW/cm}^2$ have also been reported [9], showing a strong dependence of I_{sat} to the quality of the graphene samples. The intraband conductivity can be safely assumed to be zero when $\mu_c \approx 0$. If graphene was not biased close to the Dirac point, then the first term of (8) would act as a non-saturable loss term, as the intraband conductivity has a much higher saturation threshold then the interband term [9]. We also note that for the interband conductivity saturation effect, we only consider saturation of losses, as phase related nonlinear effects are introduced through the inclusion of the graphene Kerr effect. See Appendix A for more details. Finally, the SA model in (8) ignores the spatial diffusion of graphene carriers [49] and, most importantly, assumes that the SA effect is instantaneous, a valid assumption for CW studies, but one that must be revisited for ultra-short pulses. Specifically, most theoretical and experimental studies find the phenomenological SA relaxation time to be around 1 ps [8], [12]. Thus, results presented in this work will be accurate in the pulsed regime for pulses as short as a few picoseconds, since in this regime SA is effectively instantaneous compared to the pulse duration. For femtosecond pulses, when the bandwidth does not permit to ignore dispersion effects, time-domain techniques must be employed (e.g. FDTD while also including the ultrafast graphene carrier dynamics with coupled rate equations.

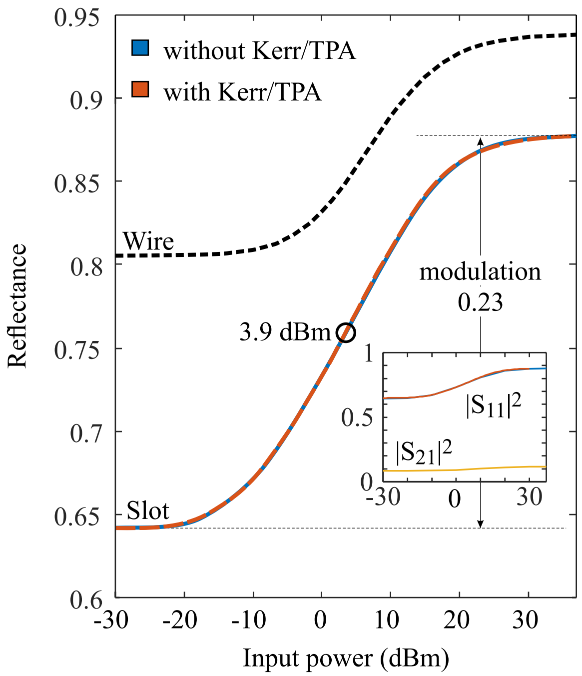

Fig. 5. Nonlinear reflectance of the silicon slot GSAM versus input power. Red and blue solid curves show the reflectance with and without Kerr/TPA, respectively. Blue and red curves coincide for input powers up to 35 dBm, without evidence for the onset of the TPA effect (contrary to the wire GSAM). For comparison purposes, dashed black curves show the reflectance of the wire GSAM, which makes evident the much higher light-graphene interaction in the slot GSAM. The bottom inset shows the transmittance, which has negligible variation with input power. The saturation power of the GSAM is denoted next to its respective point (black circle) of the reflectance curve.

Combining (7) and (8), the total graphene current density can be written as

$$\mathbf{J}_{\text{s}} = \sigma_{\text{intra}}\mathbf{E}_{\parallel} + \frac{\sigma_{\text{inter}}}{1 + \dfrac{|\mathbf{E}_{\parallel}|^2}{E_{\text{sat}}^2}}\mathbf{E}_{\parallel} + \frac{1}{4}\sigma_{xxxx}^{(3)}\left(2|\mathbf{E}_{\parallel}|^2\mathbf{E}_{\parallel} + \mathbf{E}_{\parallel}^2\mathbf{E}_{\parallel}^*\right), \tag{10}$$

which is computed only on the graphene sheet.

IV. NONLINEAR REFLECTANCE AND TRANSMITTANCE

In this section we will present the nonlinear reflectance for the two cases of GSAMs we presented so far, the wire and slot Bragg gratings. We analyze the structures with full-wave 3D FEM simulations, including all the relevant nonlinear effects, as discussed in Section III.

First, we plot in Fig. 4 the reflectance ($|S_{11}|^2$) and transmittance ($|S_{21}|^2$) versus input power for the wire Bragg grating. We observe that as the input power increases so does the reflectance. This is attributed solely to graphene's SA, as we also plot the reflectance without including Kerr/TPA effects, and we observe that the two curves coincide for input powers up to 35 dBm. For greater incident powers, we can notice in the bottom inset a slight decrease in reflectance, which signifies the onset of the TPA effect. The reason why SA is the dominant effect, is that graphene's SA develops at a much lower power threshold than

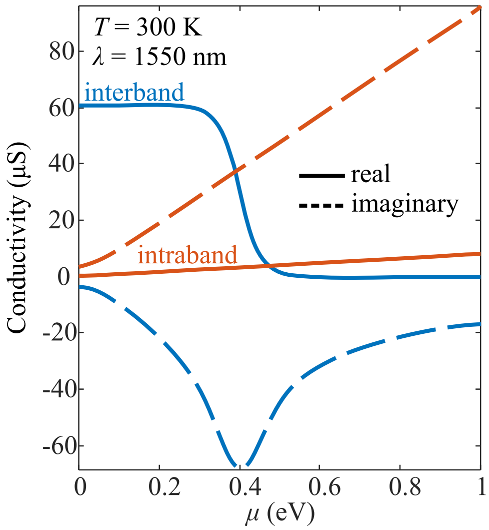

Fig. 6. Intraband and interband linear surface conductivity of a graphene sheet versus chemical potential. Conductivity is calculated for the free space wavelength of 1550 nm and a temperature of 300 K.

that of the Kerr/TPA effect [50]. Furthermore, on the leftmost inset we plot the transmittance, which shows no significant variance with power, verifying the operation as that of a saturable mirror. Finally, we define the saturation power as the CW input power needed to increase reflectance by half the maximum modulation, equal to 0.13, which for the silicon wire GSAM is calculated to be 7 dBm.

We now calculate the reflectance and transmittance versus input power for the silicon slot GSAM. The results are plotted in Fig. 5. We can again verify that the operation of the GSAM is based solely on graphene's SA, and the Kerr/TPA effects play a very marginal role. Also, again the transmittance does not exhibit significant dependence on the input power. Compared to the silicon wire GSAM, there are some significant differences, which can all be understood by the much higher light-graphene interaction and light confinement in the silicon slot GSAM [2], [29]. Firstly, the reflectance modulation is almost doubled, and the saturation power is halved (found to be around 3.9 dBm). The trade-off is that the increased interaction results into higher losses at low power as well as lower maximum reflectance. In Fig. 5, the black dashed curve shows the reflectance of the silicon wire GSAM from Fig. 4, so that one can immediately observe all of the differences that we just described. Increasing the number of Bragg periods will increase the maximum reflectance (in the high-power regime), but will simultaneously decrease the minimum reflectance (in the low power regime) and increase the required saturation power, due to the higher interaction length with graphene. Also, keep in mind that for the lasing process to start, the gain per round-trip must be greater than the losses at low power. Thus, considering the $\sim 2\,\mathrm{dB}$ ILs at lower power of our slot GSAM (no scattering losses included), an experimentally reported gain of $4\,\mathrm{dB/mm}$ in a SOH waveguide [36] and typical $1\,\mathrm{dB/mm}$ losses of a slot waveguide [51], we can roughly estimate that a laser cavity of a few millimeters will be required. One a final note, for the range of input powers that we used in Fig. 5 we did not observe any notable impact of the Kerr/TPA effects on the silicon slot GSAM response. This is attributed to the fact that in the silicon slot waveguide light is predominately guided in the slot area which is filled with PMMA. Thus, the silicon TPA effect is much weaker than in the silicon wire GSAM. Furthermore, for the same reason we expect silicon free carrier effects (which were not included in this work) to have a minimal impact to the silicon slot GSAM operation [29].

V. CONCLUSION

In this work we presented the analysis and theoretical study of two graphene enhanced silicon Bragg gratings, for the purpose of designing integrated and CMOS compatible graphene saturable absorber mirrors. The underlying waveguides were based on the silicon wire and silicon slot archetypes, and the index modulation for the formation of the Bragg mirror was achieved by periodically opening holes in the silicon waveguides. The Bragg gratings were properly designed so that the photonic bandgap was centered at the wavelength of 1550 nm with very high 3-dB bandwidth and low insertion losses. The graphene monolayer transferred on top of the planarized Bragg gratings provides the saturable absorption effect, leading to a power dependent modulation of the reflectance and effectively forming a graphene saturable absorber mirror. In all cases we verified that the modulation of the reflectance is the result of the graphene SA and not the impact of other underlying nonlinear effects, such as the silicon Kerr/TPA effects or the graphene Kerr effect. All these parasitic effects have much higher power thresholds than graphene SA, and thus do not impact the device operation for input power up to 35 dBm.

We compared the silicon wire and silicon slot GSAMs and found that the latter provides higher modulation depth of the reflectance as well as lower saturation power, with the trade-off of reasonably increased insertion losses. An added benefit of the silicon slot GSAM is that light is not strongly guided in the silicon, thus avoiding silicon's free carrier effects. Finally, our analysis was based on CW excitation, but due to graphene's ultra-fast SA dynamics our results can be readily applied to pulses as low as a few picoseconds. To the best of our knowledge, graphene saturable absorber mirrors have never been studied before in the context of Bragg gratings written in silicon and this work showcases the potential of this design for integrated mode-locking applications.

APPENDIX

A. SUMMARY OF MATERIAL PROPERTIES

The graphene-on-silicon waveguides were designed based on the linear characteristics of the materials that make up the underlying waveguides. Figure 6 shows the linear graphene conductivity at 1550 nm versus graphene's chemical potential based on [52], [53]. The Sellmeier formulae for Silicon and Silicon oxide are given below [54]:

$$n_{\mathrm{Si}}^2 - 1 = \frac{0.6961663\lambda^2}{\lambda^2 - 0.0684043^2} + \frac{0.4079426\lambda^2}{\lambda^2 - 0.1162414^2}$$

TABLE I
SUMMARY OF NONLINEAR PROPERTIES FOR SILICON AND GRAPHENE

	Kerr ($n_2, \sigma^{(3)}$)	TPA	SA (I_{sat})
Silicon	$2.5\ \mathrm{m}^2/\mathrm{W}$	$0.25n_2$	-
Graphene	$-j1.57 \cdot 10^{-21}\ \mathrm{Sm}^2/\mathrm{V}^2$	-	$1\ \mathrm{MW/cm}^2$

$$+ \frac{0.8974794\lambda^2}{\lambda^2 - 9.896161^2}, \tag{11a}$$

$$n^2_{\mathrm{SiO}_2} - 1 = \frac{10.6684293\lambda^2}{\lambda^2 - 0.301516485^2} + \frac{0.0030434748\lambda^2}{\lambda^2 - 1.13475115^2}$$

$$+ \frac{1.54133408\lambda^2}{\lambda^2 - 1104^2}, \tag{11b}$$

where in the above expressions the free-space wavelength λ is in μm. The PMMA refractive index was set at a constant 1.477. We assume that graphene is biased at a chemical potential of 0 eV, and thus ignore the intraband component of graphene's conductivity. Furthermore, we only consider the real part of the interband component. These assumptions are justified by Fig. 6, where we can see that the interband component and the imaginary part of the intraband component are very small compared to the real part of the intraband component, and thus the former will play a negligible role in the operation of the device.

Table I summarizes the nonlinear parameters for all relevant materials. The approximations to the linear conductivity also affect how SA is modeled [see (8)]. The first approximation $\sigma_{\text{intra}} \approx 0$ means that there are no non-saturable losses. The second approximation (purely real σ_{inter}) implies that the SA in graphene only affects the absorption of light. This is not entirely true, as the band filling effect, that is the basis for the SA effect, also affects the imaginary part of the conductivity [43]. In the frame of this work its effect is negligible in the linear regime, as discussed. Moreover, this refractive effect is introduced in our model indirectly through the Kerr effect [26]. Thus, although SA only affects absorption the refractive effect with increasing guided power is still taken into account by the third order nonlinear conductivity. On a final note on graphene SA, the presence of non-saturable losses from any source (e.g. waveguide fabrication imperfections, graphene impurities, biasing of graphene away from the Dirac point) as well as the fact that the reported values of I_{sat} vary in the range of $1 - 100\,\mathrm{MW/cm}^2$ [9] can considerably increase the required optical power to saturate a graphene absorber [42].

References

[1] Q. Cheng, M. Bahadori, M. Glick, S. Rumley, and K. Bergman, "Recent advances in optical technologies for data centers: A review," *Optica*, vol. 5, no. 11, Oct. 2018, Art. no. 1354. [Online]. Available: https://doi.org/10.1364/optica.5.001354

[2] F. Vogelbacher *et al.*, "Slot-waveguide silicon nitride organic hybrid distributed feedback laser," *Sci. Rep.*, vol. 9, no. 1, Dec. 2019, Art. no. 18438. [Online]. Available: https://doi.org/10.1038/s41598-019-54655-4

[3] F. Vogelbacher *et al.*, "Integrated silicon nitride organic hybrid DFB laser with inkjet printed gain medium," *Opt. Exp.*, vol. 27, no. 20, Sep. 2019, Art. no. 29350. [Online]. Available: https://doi.org/10.1364/oe.27.029350

[4] N. Tsutsumi, K. Kaida, K. Kinashi, and W. Sakai, "High-performance all-organic DFB and DBR waveguide laser with various grating height fabricated by a two-photon absorption DLW method," *Sci. Rep.*, vol. 9, no. 1, Jul. 2019, Art. no. 10582. [Online]. Available: https://doi.org/10.1038/s41598-019-47098-4

[5] D. Kohler, I. Allegro, S. F. Wondimu, L. Hahn, W. Freude, and C. Koos, "Lasing in $\mathrm{Si}_3\mathrm{N}_4$-organic hybrid (SiNOH) waveguides," *Opt. Exp.*, vol. 28, no. 4, Feb. 2020, Art. no. 5085. [Online]. Available: https://doi.org/10.1364/oe.381572

[6] X. Peng and Y. Yan, "Graphene saturable absorbers applications in fiber lasers," *J. Eur. Opt. Soc.-Rapid Pub.*, vol. 17, no. 1, Aug. 2021, Art. no. 16. [Online]. Available: https://doi.org/10.1186/s41476-021-00163-w

[7] T. Jiang *et al.*, "Ultrafast fiber lasers mode-locked by two-dimensional materials: Review and prospect," *Photon. Res.*, vol. 8, no. 1, pp. 78–90, Dec. 2019. [Online]. Available: https://doi.org/10.1364/prj.8.000078

[8] E. Malic, T. Winzer, E. Bobkin, and A. Knorr, "Microscopic theory of absorption and ultrafast many-particle kinetics in graphene," *Phys. Rev. B*, vol. 84, no. 20, Nov. 2011, Art. no. 205406. [Online]. Available: https://doi.org/10.1103/physrevb.84.205406

[9] A. Marini, J. D. Cox, and F. J. G. de Abajo, "Theory of graphene saturable absorption," *Phys. Rev. B*, vol. 95, no. 12, Mar. 2017, Art. no. 125408. [Online]. Available: https://doi.org/10.1103/physrevb.95.125408

[10] J. hui Chen, Y. Feng Xiong, F. Xu, and Y. Qing Lu, "Silica optical fiber integrated with two-dimensional materials: Towards opto-electro-mechanical technology," *Light: Sci. Appl.*, vol. 10, no. 1, pp. 1–18, Apr. 2021. [Online]. Available: https://doi.org/10.1038/s41377-021-00520-x

[11] N. Vermeulen, "Perspectives on nonlinear optics of graphene: Opportunities and challenges," *APL Photon.*, vol. 7, no. 2, Feb. 2022, Art. no. 020901. [Online]. Available: https://doi.org/10.1063/5.0082728

[12] Q. Bao *et al.*, "Atomic-layer graphene as a saturable absorber for ultrafast pulsed lasers," *Adv. Funct. Mater.*, vol. 19, no. 19, pp. 3077–3083, Oct. 2009. [Online]. Available: https://doi.org/10.1002/adfm.200901007

[13] Q. Bao *et al.*, "Monolayer graphene as a saturable absorber in a mode-locked laser," *Nano Res.*, vol. 4, no. 3, pp. 297–307, Dec. 2010. [Online]. Available: https://doi.org/10.1007/s12274-010-0082-9

[14] A. Martinez and S. Yamashita, "10 GHz fundamental mode fiber laser using a graphene saturable absorber," *Appl. Phys. Lett.*, vol. 101, no. 4, Jul. 2012, Art. no. 041118. [Online]. Available: https://doi.org/10.1063/1.4739512

[15] Z. T. Wang, Y. Chen, C. J. Zhao, H. Zhang, and S. C. Wen, "Switchable dual-wavelength synchronously Q-switched erbium-doped fiber laser based on graphene saturable absorber," *IEEE Photon. J.*, vol. 4, no. 3, pp. 869–876, Jun. 2012. [Online]. Available: https://doi.org/10.1109/jphot.2012.2199102

[16] H. Ahmad, A. Z. Zulkifli, K. Thambiratnam, and S. W. Harun, "2.0-μm Q-switched thulium-doped fiber laser with graphene oxide saturable absorber," *IEEE Photon. J.*, vol. 5, no. 4, Aug. 2013, Art. no. 1501108. [Online]. Available: https://doi.org/10.1109/jphot.2013.2273733

[17] A.-P. Luo *et al.*, "Microfiber-based, highly nonlinear graphene saturable absorber for formation of versatile structural soliton molecules in a fiber laser," *Opt. Exp.*, vol. 22, no. 22, Oct. 2014, Art. no. 27019. [Online]. Available: https://doi.org/10.1364/oe.22.027019

[18] E. J. Lee *et al.*, "Active control of all-fibre graphene devices with electrical gating," *Nature Commun.*, vol. 6, no. 1, Apr. 2015, Art. no. 6851. [Online]. Available: https://doi.org/10.1038/ncomms7851

[19] R. Zhang *et al.*, "Tunable Q-switched fiber laser based on a graphene saturable absorber without additional tuning element," *IEEE Photon. J.*, vol. 11, no. 1, Feb. 2019, Art. no. 1500310. [Online]. Available: https://doi.org/10.1109/jphot.2019.2892646

[20] J. D. Zapata, D. Steinberg, L. A. M. Saito, R. E. P. de Oliveira, A. M. Cárdenas, and E. A. T. de Souza, "Efficient graphene saturable absorbers on D-shaped optical fiber for ultrashort pulse generation," *Sci. Rep.*, vol. 6, no. 1, Feb. 2016, Art. no. 20644. [Online]. Available: https://doi.org/10.1038/srep20644

[21] S. Wang, X. Sun, Y. Luo, and G. Peng, "Surface plasmon resonance sensor based on D-shaped Hi-Bi photonic crystal fiber," *Opt. Commun.*, vol. 467, Jul. 2020, Art. no. 125675. [Online]. Available: https://doi.org/10.1016/j.optcom.2020.125675

[22] A. K. Pathak and V. K. Singh, "Theoretical assessment of D-shaped optical fiber chemical sensor associated with nanoscale silver strip operating in near-infrared region," *Opt. Quantum Electron.*, vol. 52, no. 4, Mar. 2020, Art. no. 199. [Online]. Available: https://doi.org/10.1007/s11082-020-02316-6

[23] D. Chatzidimitriou, A. Pitilakis, and E. E. Kriezis, "Rigorous calculation of nonlinear parameters in graphene-comprising waveguides," *J. Appl. Phys.*, vol. 118, no. 2, Jul. 2015, Art. no. 023105. [Online]. Available: https://doi.org/10.1063/1.4926501

[24] A. Pitilakis, D. Chatzidimitriou, and E. E. Kriezis, “Theoretical and numerical modeling of linear and nonlinear propagation in graphene waveguides,” *Opt. Quantum Electron.*, vol. 48, no. 4, Mar. 2016, Art. no. 243. [Online]. Available: https://doi.org/10.1007/s11082-016-0510-5

[25] K. Alexander, N. A. Savostianova, S. A. Mikhailov, D. V. Thourhout, and B. Kuyken, “Gate-tunable nonlinear refraction and absorption in graphene-covered silicon nitride waveguides,” *ACS Photon.*, vol. 5, no. 12, pp. 4944–4950, Nov. 2018. [Online]. Available: https://doi.org/10.1021/acsphotonics.8b01132

[26] P. Demongodin *et al.*, “Ultrafast saturable absorption dynamics in hybrid graphene $\mathrm{Si_3N_4}$ waveguides,” *APL Photon.*, vol. 4, no. 7, Jul. 2019, Art. no. 076102. [Online]. Available: https://doi.org/10.1063/1.5094523

[27] Y. Qu *et al.*, “Enhanced four-wave mixing in silicon nitride waveguides integrated with 2D layered graphene oxide films,” *Adv. Opt. Mater.*, vol. 8, no. 23, Oct. 2020, Art. no. 2001048. [Online]. Available: https://doi.org/10.1002/adom.202001048

[28] M. Grande *et al.*, “Absorption and losses in one-dimensional photonic-crystal-based absorbers incorporating graphene,” *IEEE Photon. J.*, vol. 6, no. 6, Dec. 2014, Art. no. 0600808. [Online]. Available: https://doi.org/10.1109/jphot.2014.2356495

[29] Z. Jafari, A. Zarifkar, M. Miri, and L. Zhang, “All-optical modulation in a graphene-covered slotted silicon nano-beam cavity,” *J. Lightw. Technol.*, vol. 36, no. 18, pp. 4051–4059, Sep. 2018. [Online]. Available: https://doi.org/10.1109/jlt.2018.2858551

[30] T. Christopoulos, O. Tsilipakos, and E. E. Kriezis, “Low-power bistability in graphene-comprising 3D photonic resonant circuits,” *J. Appl. Phys.*, vol. 122, no. 23, Dec. 2017, Art. no. 233101. [Online]. Available: https://doi.org/10.1063/1.5005610

[31] J. Capmany, D. Domenech, and P. Muñoz, “Silicon graphene Bragg gratings,” *Opt. Exp.*, vol. 22, no. 5, Feb. 2014, Art. no. 5283. [Online]. Available: https://doi.org/10.1364/oe.22.005283

[32] C. A. Zaugg *et al.*, “Ultrafast and widely tuneable vertical-external-cavity surface-emitting laser, mode-locked by a graphene-integrated distributed Bragg reflector,” *Opt. Exp.*, vol. 21, no. 25, Dec. 2013, Art. no. 31548. [Online]. Available: https://doi.org/10.1364/oe.21.031548

[33] G. Q. Xie *et al.*, “Graphene saturable absorber for Q-switching and mode locking at 2 μm wavelength,” *Opt. Mater. Exp.*, vol. 2, no. 6, pp. 878–883, May 2012. [Online]. Available: https://doi.org/10.1364/ome.2.000878

[34] J.-L. Xu, X.-L. Li, Y.-Z. Wu, X.-P. Hao, J.-L. He, and K.-J. Yang, “Graphene saturable absorber mirror for ultra-fast-pulse solid-state laser,” *Opt. Lett.*, vol. 36, no. 10, pp. 1948–1950, May 2011. [Online]. Available: https://doi.org/10.1364/ol.36.001948

[35] Y. Wang *et al.*, “Passively mode-locked solid-state laser with absorption tunable graphene saturable absorber mirror,” *J. Lightw. Technol.*, vol. 37, no. 13, pp. 2927–2931, Jul. 2019. [Online]. Available: https://doi.org/10.1109/jlt.2019.2907654

[36] D. Korn *et al.*, “Lasing in siliconorganic hybrid waveguides,” *Nature Commun.*, vol. 7, no. 1, Mar. 2016, Art. no. 10864. [Online]. Available: https://doi.org/10.1038%2Fncomms10864

[37] X. Wang, S. Grist, J. Flueckiger, N. A. F. Jaeger, and L. Chrostowski, “Silicon photonic slot waveguide Bragg gratings and resonators,” *Opt. Exp.*, vol. 21, no. 16, pp. 19029–19039, Aug. 2013. [Online]. Available: https://doi.org/10.1364/oe.21.019029

[38] W. Fuscaldo *et al.*, “Terahertz characterization of graphene conductivity via time-domain reflection spectroscopy on metal-backed dielectric substrates,” *J. Phys. D: Appl. Phys.*, vol. 55, no. 36, Jun. 2022, Art. no. 365101. [Online]. Available: https://doi.org/10.1088/1361-6463/ac7759

[39] T. Stauber, N. M. R. Peres, and A. K. Geim, “Optical conductivity of graphene in the visible region of the spectrum,” *Phys. Rev. B*, vol. 78, no. 8, Aug. 2008, Art. no. 085432. [Online]. Available: https://doi.org/10.1103/physrevb.78.085432

[40] A. Phatak, Z. Cheng, C. Qin, and K. Goda, “Design of electro-optic modulators based on graphene-on-silicon slot waveguides,” *Opt. Lett.*, vol. 41, no. 11, pp. 2501–2504, May 2016. [Online]. Available: https://doi.org/10.1364/ol.41.002501

[41] A. D’Arco *et al.*, “Fabrication and spectroscopic characterization of graphene transparent electrodes on flexible cyclo-olefin substrates for terahertz electro-optic applications,” *Nanotechnology*, vol. 31, no. 36, Jun. 2020, Art. no. 364006. [Online]. Available: https://doi.org/10.1088/1361-6528/ab96e6

[42] J. Wang *et al.*, “Saturable absorption in graphene-on-waveguide devices,” *Appl. Phys. Exp.*, vol. 12, no. 3, Feb. 2019, Art. no. 032003. [Online]. Available: https://doi.org/10.7567/1882-0786/ab02ca

[43] N. Vermeulen *et al.*, “Graphene’s nonlinear-optical physics revealed through exponentially growing self-phase modulation,” *Nature Commun.*, vol. 9, no. 1, Jul. 2018, Art. no. 2675. [Online]. Available: https://doi.org/10.1038/s41467-018-05081-z

[44] Z. Sun *et al.*, “Graphene mode-locked ultrafast laser,” *ACS Nano*, vol. 4, no. 2, pp. 803–810, Jan. 2010. [Online]. Available: https://doi.org/10.1021/nn901703e

[45] J. Wang *et al.*, “High-responsivity graphene-on-silicon slot waveguide photodetectors,” *Nanoscale*, vol. 8, no. 27, pp. 13206–13211, 2016. [Online]. Available: https://doi.org/10.1039/c6nr03122f

[46] R. W. Boyd, “The intensity-dependent refractive index,” in *Nonlinear optics*, R. W. Boyd Ed., Burlington, VT, USA: Academic Press, 2008, ch. 4, pp. 207–252. [Online]. Available: https://www.sciencedirect.com/science/article/pii/B9780123694706000046

[47] B. A. Daniel and G. P. Agrawal, “Vectorial nonlinear propagation in silicon nanowire waveguides: Polarization effects,” *J. Opt. Soc. Amer. B*, vol. 27, no. 5, pp. 956–965, Apr. 2010. [Online]. Available: https://doi.org/10.1364/josab.27.000956

[48] N. Vermeulen *et al.*, “Negative kerr nonlinearity of graphene as seen via chirped-pulse-pumped self-phase modulation,” *Phys. Rev. Appl.*, vol. 6, no. 4, Oct. 2016, Art. no. 044006. [Online]. Available: https://doi.org/10.1103/physrevapplied.6.044006

[49] D. Chatzidimitriou and E. E. Kriezis, “Light propagation in nanophotonic waveguides considering graphenes saturable absorption,” *Phys. Rev. A*, vol. 102, no. 5, Nov. 2020, Art. no. 053512. [Online]. Available: https://doi.org/10.1103/physreva.102.053512

[50] A. Pitilakis, D. Chatzidimitriou, T. V. Yioultsis, and E. E. Kriezis, “Asymmetric Si-slot coupler with nonreciprocal response based on graphene saturable absorption,” *IEEE J. Quantum Electron.*, vol. 57, no. 3, Jun. 2021, Art. no. 8400210. [Online]. Available: https://doi.org/10.1109/jqe.2021.3071247

[51] T. Vallaitis *et al.*, “Optical properties of highly nonlinear silicon-organic hybrid (SOH) waveguide geometries,” *Opt. Exp.*, vol. 17, no. 20, Sep. 2009, Art. no. 17357. [Online]. Available: https://doi.org/10.1364/oe.17.017357

[52] L. A. Falkovsky, “Optical properties of graphene,” *J. Phys.: Conf. Ser.*, vol. 129, Oct. 2008, Art. no. 012004. [Online]. Available: https://doi.org/10.1088/1742-6596/129/1/012004

[53] G. W. Hanson, “Dyadic greens functions for an anisotropic, non-local model of biased graphene,” *IEEE Trans. Antennas Propag.*, vol. 56, no. 3, pp. 747–757, Mar. 2008. [Online]. Available: https://doi.org/10.1109/tap.2008.917005

[54] L. Zhang, A. M. Agarwal, L. C. Kimerling, and J. Michel, “Nonlinear group IV photonics based on silicon and germanium: From near-infrared to mid-infrared,” *Nanophotonics*, vol. 3, no. 4/5, pp. 247–268, Aug. 2014. [Online]. Available: https://doi.org/10.1515/nanoph-2013-0020